Jahn-Teller effect in the $^4T_1$ state of Mn^{2+} in GaP

G. Hofmann
Max-Planck-Institut für Festkörperforschung, Heisenbergstrasse 1, 7000 Stuttgart 80, Federal Republic of Germany

F. G. Anderson
Laboratoire de Physique des Solides, Institut Supérieur d'Electronique du Nord, 41 boulevard Vauban, F-59046 Lille CEDEX, France

J. Weber
Max-Planck-Institut für Festkörperforschung, Heisenbergstrasse 1, 7000 Stuttgart 80, Federal Republic of Germany

(Received 29 October 1990)

Uniaxial-stress and Zeeman experiments of the manganese-induced zero-phonon lines in GaP:Mn are presented. An analysis of the data indicates that the zero-phonon transitions are due to the $^4T_1$-$^6A_1$ internal transition of $Mn^{2+}(3d^5)$. From the unperturbed spectra, as well as from the splittings of the zero-phonon lines, we are able to deduce that the $^4T_1$ state couples to distortions with ε symmetry. The Jahn-Teller effect in the static limit determines the interaction of the $^4T_1$ state with the ε modes of distortion. Based on a comparison between the calculated and experimentally derived splittings and intensities, we find perfect agreement between theory and experiment.

I. INTRODUCTION

Manganese-doped GaP gives rise to a characteristic photoluminescence (PL) band consisting of a zero-phonon (ZP) line at 1.534 eV followed by a phonon sideband with a maximum at 1.34 eV. Vink and Van Gorkom ascribed the origin of this PL band to the $^4T_1$-$^6A_1$ internal transitions of Mn^{2+}.[1] At approximately 10 K, a hot line separated by 1.2 meV from the ZP line is observed.[1] No further ZP lines are detected at higher temperatures. Similar results were found in the Mn-doped II-VI compounds ZnS,[2] ZnSe,[3] and CdS.[3] In all cases, only two ZP lines of the $^4T_1$-$^6A_1$ transition are detected. However, crystal-field theory, including second-order spin-orbit interaction, predicts four ZP lines.

Koidl performed a theoretical investigation of several triplet states of Mn^{2+}, based on the hypothesis of a strong Jahn-Teller coupling in Ref. 4. The occurrence of only two ZP lines was explained as being due to the quenching of the first-order spin-orbit interaction in the $^4T_1$ state by the Jahn-Teller effect. The Zeeman effect and the magnetic polarization of the $^4T_1$-$^6A_1$ transition of Mn^{2+} in ZnS were investigated,[5] and uniaxial-stress experiments in ZnSe and ZnS (Ref. 6) were performed. The splitting and the intensities of the ZP lines were calculated under the assumption of a strong Jahn-Teller coupling to the ε-mode distortions and were found to be in good agreement with the experimental data.

The purpose of our work is to verify, by uniaxial-stress and Zeeman experiments, the $^4T_1$-$^6A_1$ internal transition of Mn^{2+} in GaP and to determine the strong coupling to distortions of ε symmetry in the $^4T_1$ state.

II. EXPERIMENT

Samples were cut for the uniaxial-stress experiments from an n-type liquid-encapsulated-Czochralski-grown crystal with a Mn concentration of approximately 1×10^{17} cm^3. The samples were orientated along the three main crystallographic axes. A GaP layer doped with Mn and grown by vapor-phase epitaxy (VPE) with a Mn concentration of approximately 5×10^{18} cm^3 was used for the magnetic-field measurements. The thickness of the layer was approximately 300 μm with a (100) orientation.

The uniaxial-stress experiments were performed at 4.2 K in an optical cryostat with the samples immersed in liquid He. The samples were mounted at room temperature between two metal pistons which were part of the sample holder. The stress was applied to the sample using an arrangement consisting of a calibrated high-tension spring adjusted by a screw to control the pressure applied between the two metal pistons. The uniaxial stress was calculated from the force indicated by the spring divided by the sample areas. The offset of the stress due to static friction could not be determined experimentally. In order to perform uniaxial-stress experiments at higher temperatures, the He level was kept below the sample, giving a sample temperature of approximately 20 K.

The Zeeman experiments were carried out with a superconducting split-coil magnet with a maximum magnetic field of 7 T. The samples were immersed in liquid He. For measurements at higher temperatures, the cryomagnetic system allowed the sample temperature to

be varied up to 300 K. All spectra were taken in the Voigt configuration ($\mathbf{H}\perp\mathbf{k}$, where $\mathbf{k}$ denotes the propagation vector of the detected light).

The PL was excited by the 514.5-nm line of an Ar^+ laser for both the uniaxial-stress and the Zeeman experiments. The PL signal was dispersed by a 1-m grating monochromator (SPEX Industries) and detected by a cooled GaAs photomultiplier.

III. EXPERIMENTAL RESULTS

A. Unperturbed spectra

A spectrum of the ZP lines A and B in GaP:Mn is shown in Fig. 1. At 4.2 K only one ZP line (A) is detected at 1.5340 eV, whereas at higher temperatures a second ZP line (B) appears at 1.5352 eV. The separation between the two ZP lines is 1.2 meV. This is in contrast to the value of 1.4 meV reported in Ref. 1. From the relative intensities of the lines A and B at different temperatures we conclude that the splitting arises from the excited PL state and that the transitions A and B have the same final state. At temperatures higher than 25 K, both ZP lines show a considerable broadening and at $T>40$ K the lines could no longer be detected.

B. Uniaxial-stress splitting

The developments of the uniaxial-stress splittings of lines A and B for $\mathbf{P}\|[111]$, $\mathbf{P}\|[001]$, and $\mathbf{P}\|[110]$ with uniaxial stress up to 90 MPa are shown in Figs. 2, 3, and 4, respectively. Lines A and B do not split for $\mathbf{P}\|[111]$. Both lines shift linearly to lower energies at the same rate. Uniaxial stress along the [001] or [110] crystal directions gives rise to a linear twofold splitting of lines A and B. For the following, the components of line A and B will be labeled A_z, A_{xy}, B_z, and B_{xy} (as shown in Figs. 3 and 4). The dotted lines in Figs. 3 and 4 represent the shift of lines A and B with stress along the [111] direction. With respect to these lines, A_z and B_z shift at twice the rate as the components A_{xy} and B_{xy}. For any

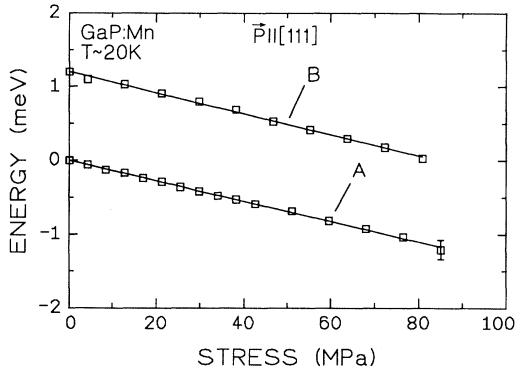

FIG. 2. Shift of the ZP lines A and B for uniaxial stress $\mathbf{P}\|[111]$. The zero of energy is at the position of the ZP line A without stress.

given stress, the splitting between the components A_z and A_{xy}, or that between B_z and B_{xy}, is nearly twice as large for [001] stress as for [110] stress. No coupling between the stress-split components of lines A and B is observed. The various lines thermalize according to their energy separation, indicating that the splitting occurs entirely in the excited state.

The polarization behavior of lines A_z and A_{xy} for uniaxial stress along the [001] and [110] directions at $P=40$ MPa and $T=4.2$ K is given in Fig. 5. For $\mathbf{P}\|[001]$ and $\mathbf{E}\|\mathbf{P}$ line A_z disappears. For $\mathbf{E}\perp\mathbf{P}$ the integrated intensities of the two components are equal, when the intensities are corrected for the thermalization in the initial state of the optical transitions, as shown in Fig. 5 by the vertical bars. Two cases have to be distinguished for $\mathbf{P}\|[110]$. If $\mathbf{k}\|[001]$, then for both $\mathbf{E}\|\mathbf{P}$ and $\mathbf{E}\perp\mathbf{P}$ the integrated intensities are again equal, when corrected for the thermalization. However, for $\mathbf{k}\|[1\bar{1}0]$, the component A_z disappears for $\mathbf{E}\perp\mathbf{P}$, but for $\mathbf{E}\|\mathbf{P}$ the integrated intensities are

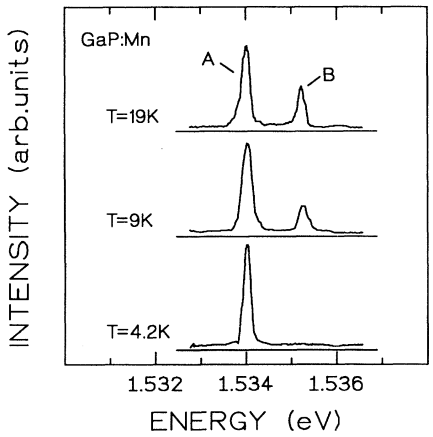

FIG. 1. Photoluminescence spectra recorded with increasing temperature in the region of the ZP line. At $T=9$ K, a second ZP line appears.

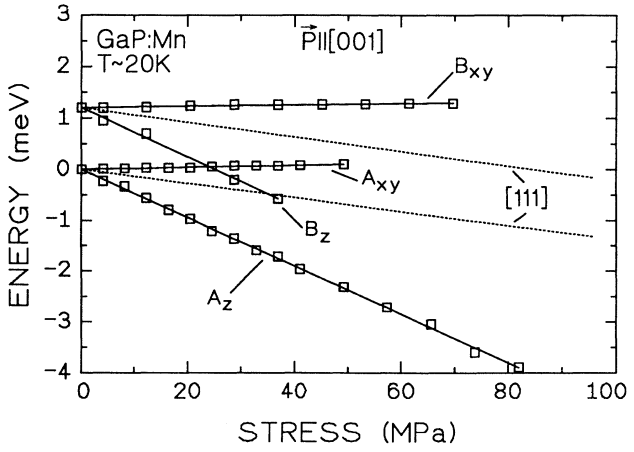

FIG. 3. Splitting of the ZP lines A and B for uniaxial stress $\mathbf{P}\|[001]$. The dotted lines represent the shift due to the ε_{a1} strain (see Fig. 2).

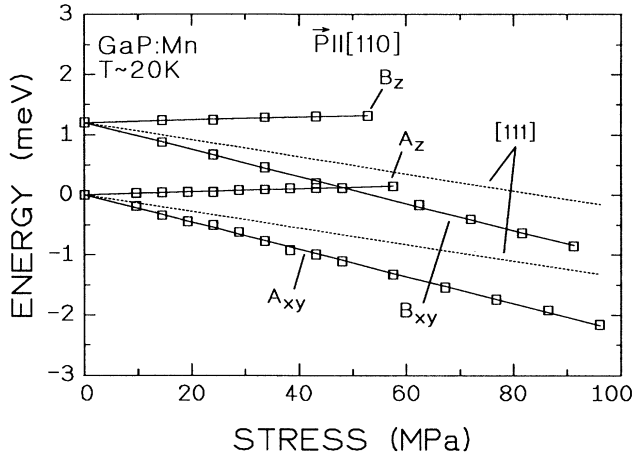

FIG. 4. Splitting of the ZP lines A and B for uniaxial stress $\mathbf{P}\|[110]$.

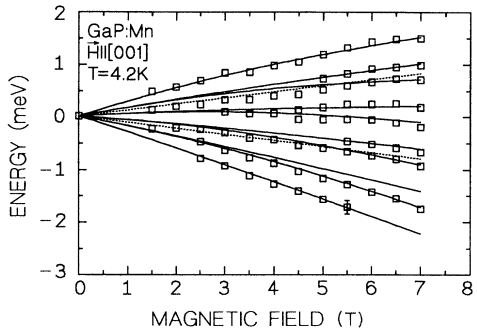

FIG. 6. Development of the Zeeman splitting of line A for a magnetic field $\mathbf{H}\|[001]$. The curves are calculated according to Eq. (5). The dotted curves are transitions associated with the z-axis distortion. Only allowed dipole transitions are shown. The zero of energy is at the position of the ZP line A without magnetic field.

identical after excluding the thermalization in the initial state. The same behavior holds for components B_z and B_{xy}, although not shown in Fig. 5.

It is evident in Fig. 5 that the stress-split components found at lower energies are broadened with respect to components found at higher energies. We do not believe that the broadening is due to the inhomogeneity of the uniaxial stress. The quality of the stress was checked by observing the broadening behavior of the nitrogen lines which were also present in the PL spectra. No noticeable broadening of these lines was detected up to 70 MPa.

C. Magnetic-field splitting

The development of the Zeeman splitting of line A for $\mathbf{H}[001]$ is shown in Fig. 6, and the corresponding 7-T spectrum in Fig. 7. The solid and dotted curves in Fig. 6 give the theoretical splitting calculated in the following section and the squares signify the experimental points. The splitting of line A for $H\|[110]$ up to 7 T is shown in Fig. 8 and the corresponding 7-T spectrum is traced in Fig. 9. The Zeeman splitting of line A for $\mathbf{H}\|[111]$ is shown in Fig. 10 and the 7-T spectrum in Fig. 11.

The Zeeman anisotropy of line A at 6.5 T, where the sample was rotated in the [110] crystallographic direction perpendicular to the magnetic field, is presented in Fig. 12. The polarization behavior for $\mathbf{E}\|\mathbf{H}$ and $\mathbf{E}\perp\mathbf{H}$ for $\mathbf{H}\|[001]$, $\mathbf{H}\|[110]$, and $\mathbf{H}\|[111]$ is depicted in Figs. 13, 14, and 15, respectively. The spectra on the right-hand side of these figures are the theoretical spectra calculated according to a model to be developed in the following section.

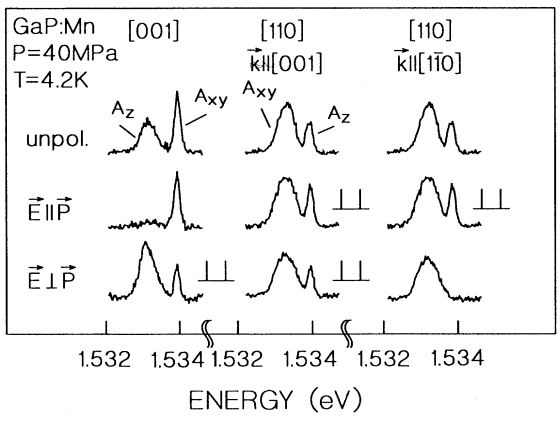

FIG. 5. Unpolarized and polarized intensities for uniaxial stress $P=40$ MPa along the [001] and [110] directions; $\mathbf{k}$ denotes the propagation vector of the detected light. The vertical bars show the integrated intensities of the stress-split components when thermalization effects are excluded.

IV. THEORETICAL MODEL

In this section, we present a model for the electronic structure of the Mn^{2+} impurity in GaP. Our model de-

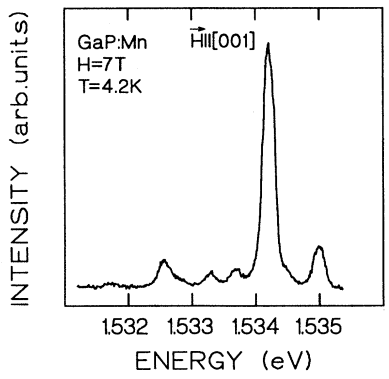

FIG. 7. Photoluminescence spectrum of line A for a magnetic field $\mathbf{H}\|[001]$ and $H=7$ T.

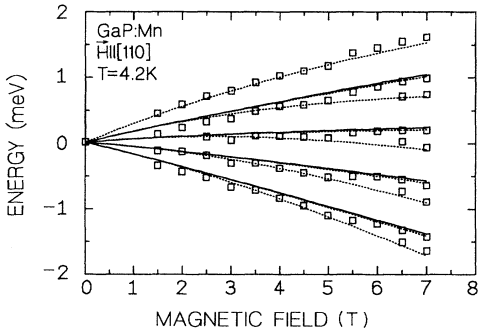

FIG. 8. Zeeman splitting of line A for increasing magnetic field $\mathbf{H}\|[110]$.

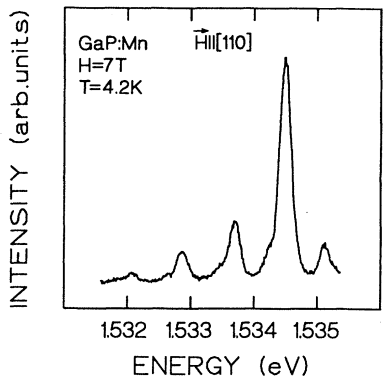

FIG. 9. Photoluminescence spectrum of line A for a magnetic field $\mathbf{H}\|[110]$ and $H=7$ T.

scribes the Jahn-Teller coupling of the $^4T_1$ excited Mn^{2+} state and is similar to that given by Koidl,[4] although we treat the effects of the Jahn-Teller coupling in a different manner. The Mn impurity assumes a 2+ charge state when it substitutes for Ga in GaP, corresponding to a d^5 configuration. The ground-state manifold for a d^5 configuration is a $^6A_1$ manifold, coming from the atomic ^6S term. The first excited state is a $^4T_1$ manifold, resulting from the crystal-field mixing of the ^4G, ^4P, and ^4F atomic terms. Electric-dipole transitions from the $^4T_1$ to the $^6A_1$ manifold become allowed only when the spin-orbit mixing between these two manifolds is included. The $^4T_1$ states that are mixed into each of the $^6A_1$ states are given in Eq. (1), in which the $^4T_1$ states are written as $|\text{orbit, spin}\rangle$ states,

$$
\begin{aligned}
|5/2\rangle &\sim (1/\sqrt{2})(-|x,3/2\rangle - i|y,\tfrac{3}{2}\rangle)\ ,\\
|3/2\rangle &\sim (1/\sqrt{10})(-\sqrt{3}|x,1/2\rangle - \sqrt{3}i|y,1/2\rangle \\
&\qquad +2|z,3/2\rangle)\ ,\\
|1/2\rangle &\sim (1/\sqrt{20})(-\sqrt{3}|x,-1/2\rangle - \sqrt{3}i|y,-1/2\rangle \\
&\qquad +\sqrt{12}|z,1/2\rangle + |x,3/2\rangle \\
&\qquad -i|y,3/2\rangle)\ ,\\
|-1/2\rangle &\sim (1/\sqrt{20})(-|x,-3/2\rangle - i|y,-3/2\rangle \\
&\qquad +\sqrt{12}|z,-1/2\rangle + \sqrt{3}|x,1/2\rangle \\
&\qquad -\sqrt{3}i|y,1/2\rangle)\ ,\\
|-3/2\rangle &\sim (1/\sqrt{10})(2|z,-3/2\rangle + \sqrt{3}|x,-1/2\rangle \\
&\qquad -\sqrt{3}i|y,-1/2\rangle)\ ,\\
|-5/2\rangle &\sim (1/\sqrt{2})(|x,-3/2\rangle - i|y,-3/2\rangle)\ .
\end{aligned}
\tag{1}
$$

The spin-orbit interaction splits the $^4T_1$ manifold into four spin-orbit manifolds, two Γ_8's, a Γ_7, and a Γ_6. The operator giving the various spin-orbit splittings between these manifolds, including second-order effects, is

$$\mathcal{H}_{\text{s.o.}} = \chi \mathcal{L}\cdot\mathbf{S} + \mu(\mathcal{L}\cdot\mathbf{S})^2 + \rho(\mathcal{L}_x^2 S_x^2 + \mathcal{L}_y^2 S_y^2 + \mathcal{L}_z^2 S_z^2)\ , \tag{2}$$

where $\mathcal{L}$ is the effective orbital momentum. For a T_1 orbital triplet, $\mathcal{L}=1$. Electric-dipole transitions between each of these four spin-orbit manifolds and the ground state are allowed. Hence, we would expect to observe four transitions. However, only two transitions are observed (see Fig. 1). This discrepancy can be readily removed when we include a Jahn-Teller coupling in the $^4T_1$ manifold. The Jahn-Teller coupling that we consider is between the T_1 orbital triplet and the ε modes of distortion.

While the descriptions given in Refs. 4 and 6 of the effects of the Jahn-Teller coupling on the spin-orbit splittings are correct, we can gain further insight into this problem by considering first the Jahn-Teller coupling and then the spin-orbit interaction (similarly as in Ref. 5, but we treat the spin-orbit interaction in a different manner). In the static $T_1\otimes\varepsilon$ Jahn-Teller problem, the lattice distorts along one of the three cubic axes, the distortion being determined by which electronic state is occupied. For example, if the occupied state has $|T_{1z}\rangle$ as its orbital part, the distortion is along the z axis. This distortion partially lifts the degeneracy of the $^4T_1$ manifold, as shown in Fig. 16. We note that the Jahn-Teller coupling does not affect the spin states. So, we still have a spin quartet, $S=\frac{3}{2}$. The energy splitting between the $^4T_{1z}$ states and the degenerate states $^4T_{1y}$ and $^4T_{1x}$ is $3E_{\text{JT}}$,

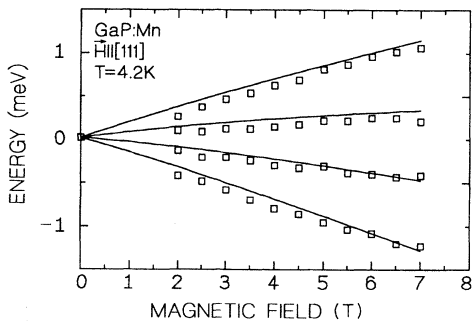

FIG. 10. Zeeman splitting of line A for increasing magnetic field $H\|[111]$.

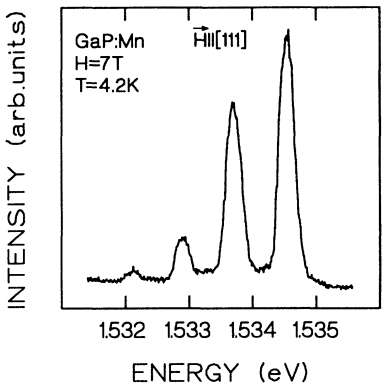

FIG. 11. Photoluminescence spectrum of line A for $\mathbf{H}[111]$ and $H=7$ T.

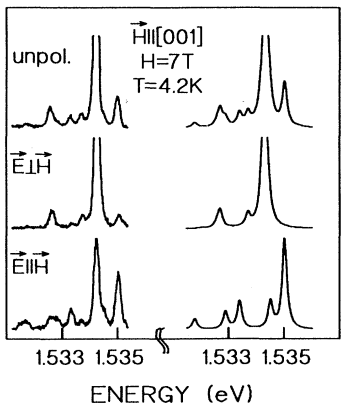

FIG. 13. Experimentally determined PL spectra for $\mathbf{H}\|[001]$ and $H=7$ T on the left-hand side are compared with the theoretical spectra on the right-hand side. In order to see the weak intensive lines some spectra are cut at half maximum intensity.

where E_{JT} is the Jahn-Teller energy. For a distortion along the x (y) axis, the resulting lowest-energy quartet is the $^4T_{1x}$ ($^4T_{1y}$).

We consider now the spin-orbit interaction for the particular case in which the Jahn-Teller distortion is along the z axis. There are no first-order spin-orbit matrix elements within the $^4T_{1z}$ quartet. There are, however, second-order effects. This second-order interaction is described by the operator

$$\mathcal{H}'_{s.o.}=A(\mathcal{L}_x^2S_x^2+\mathcal{L}_y^2S_y^2+\mathcal{L}_z^2S_z^2)\ , \tag{3}$$

where $A=\mu+\rho-\lambda^2/3E_{JT}$ with λ the many-electron spin-orbit parameter within the $^4T_1$ manifold. The constants μ and ρ are the parameters found in Eq. (2). In fact, as a result of the Jahn-Teller splittings in the $^4T_1$ manifold and any such splittings in other manifolds that are coupled to the $^4T_1$ manifold by the spin-orbit interaction, the actual values of μ and ρ are slightly different from their values in pure crystal-field theory when the Jahn-Teller coupling is neglected. This is a result of the changes, coming from the Jahn-Teller splittings, in the energy denominators found in the parameters μ and ρ. The $\mu+\rho$ contribution to A comes from the spin-orbit coupling between the $^4T_{1z}$ quartet and other manifolds, e.g., the $^6A_1$. The $-\lambda^2/3E_{JT}$ contribution to A arises from the spin-orbit interaction coupling the $^4T_{1z}$ quartet to the excited quartets $^4T_{1x}$ and $^4T_{1y}$. The net result of the spin-orbit coupling, as given by the operator in Eq. (3), is to partially lift the spin degeneracy of the $^4T_{1z}$ quartet, as shown in Fig. 16.

In general, any one of the three quartets $^4T_{1x}$, $^4T_{1y}$, and $^4T_{1z}$ can be the lowest-energy quartet, each with its own distortion axis. We note that Eq. (3) is valid for each of these quartets being the lowest-energy quartet. In Fig. 17, we show the splitting of the spin quartet for each of the three possible distortions. The states shown in Fig. 17 ($|$orbit, spin$\rangle\rangle$) are linear combinations of the states from the $^4T_1$ manifold. These combinations, written as

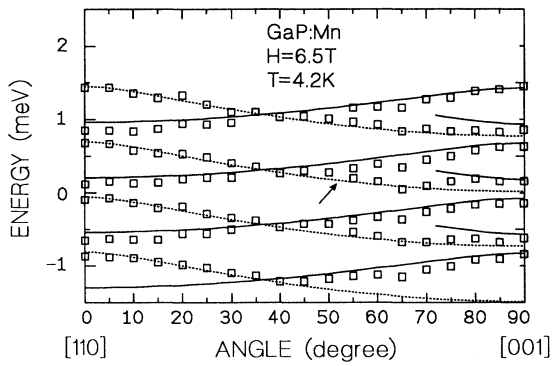

FIG. 12. Angular dependence of the most intensive Zeeman components.

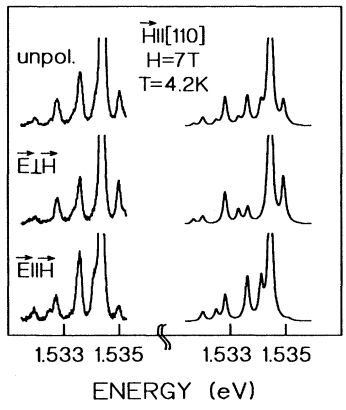

FIG. 14. Experimentally determined PL spectra for $\mathbf{H}\|[110]$ and $H=7$ T on the left-hand side are compared with the theoretical spectra on the right-hand side. In this case $\mathbf{E}\perp\mathbf{H}$ means $\mathbf{E}$ is parallel to the $[1\bar{1}0]$ direction.

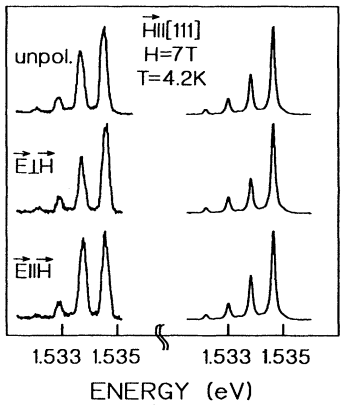

FIG. 15. Experimentally determined PL spectra for $\mathbf{H}\|[111]$ and $H=7$ T on the left-hand side are compared with the theoretical spectra on the right-hand side.

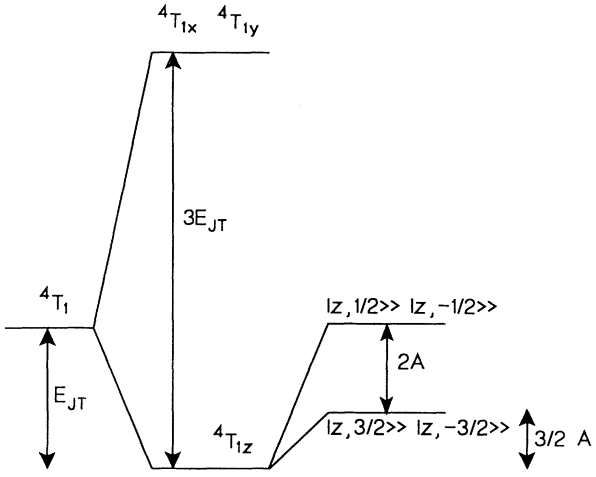

FIG. 16. Splitting of the T_1 manifold due to a static distortion along the z axis, and the splitting of the ${}^4T_{1z}$ manifold due to the second-order spin-orbit interaction.

$|\text{orbit, spin}\rangle$ states, are

$$
\begin{aligned}
|x,1/2\rangle\rangle &= \tfrac{1}{2}(|x,-3/2\rangle+\sqrt{3}|x,1/2\rangle)\,,\\
|x,-1/2\rangle\rangle &= \tfrac{1}{2}(|x,3/2\rangle+\sqrt{3}|x,-1/2\rangle)\,,\\
|x,3/2\rangle\rangle &= \tfrac{1}{2}(\sqrt{3}|x,3/2\rangle-|x,-1/2\rangle)\,,\\
|x,-3/2\rangle\rangle &= \tfrac{1}{2}(\sqrt{3}|x,-3/2\rangle-|x,1/2\rangle)\,,\\
|y,1/2\rangle\rangle &= \tfrac{1}{2}(|y,-3/2\rangle-\sqrt{3}|y,1/2\rangle)\,,\\
|y,-1/2\rangle\rangle &= \tfrac{1}{2}(|y,3/2\rangle-\sqrt{3}|y,-1/2\rangle)\,,\\
|y,3/2\rangle\rangle &= \tfrac{1}{2}(\sqrt{3}|y,3/2\rangle+|y,-1/2\rangle)\,,\\
|y,-3/2\rangle\rangle &= \tfrac{1}{2}(\sqrt{3}|y,-3/2\rangle+|y,1/2\rangle)\,,\\
|z,1/2\rangle\rangle &= |z,1/2\rangle\,,\\
|z,1/2\rangle\rangle &= |z,1/2\rangle\,,\\
|z,3/2\rangle\rangle &= |z,3/2\rangle\,,\\
|z,3/2\rangle\rangle &= |z,3/2\rangle\,.
\end{aligned}
\tag{4}
$$

Linear combinations of the six states at lower-energy span manifolds of Γ_8 and Γ_7 symmetry. The six states found $2A$ in energy above these first six states span manifolds of Γ_8 and Γ_6 symmetry. These manifolds are exactly the spin-orbit manifolds found in crystal-field theory.

However, while linear combinations of the states from the three different distortions span the various spin-orbit manifolds, in the static limit of the Jahn-Teller coupling, the states associated with different distortions are not in contact with each other. If there were a tunneling between the different distortions, which for the $T_1\otimes\varepsilon$ problem is driven by the spin-orbit interaction, there would be an associated tunneling splitting.[7] The states that are separated by the tunneling splitting are precisely the states belonging to the Γ_8 and Γ_7 manifolds for the lower-energy states, and the Γ_8 and Γ_6 manifolds for the higher-energy states. Hence, the tunneling splitting would give rise to the four distinct spin-orbit manifolds, although the ordering of these states is different than that expected from crystal-field theory. The progression of these splittings from the crystal-field limit to the static limit of Jahn-Teller coupling has been given by Koidl (see Fig. 1 of Ref. 4). Hence, we see how the four spin-orbit manifolds found in crystal-field theory merge into two states in the static limit of Jahn-Teller coupling.

V. COMPARISON WITH EXPERIMENT

A. Unperturbed spectra

In the preceding section, we have demonstrated how the four spin-orbit manifolds from the ${}^4T_1$ manifold merge into two states separated by $2A$ in energy with increasing coupling to an ε distortion. The transitions from these two states to the ${}^6A_1$ ground manifold give rise to the two luminescence lines labeled A and B in Fig. 1. From the energy difference between these two lines, we find $A=0.6$ meV. In our measurements, we have

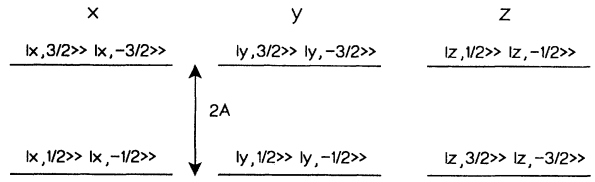

FIG. 17. Ground and first excited states of the ${}^4T_1$ manifold for static distortion along the x, y, or z axis. The states are labeled according to Eq. (4).

never observed any splittings that would result from a tunneling between the various distortions. We conclude that the Jahn-Teller coupling occurs in the static limit.

B. Uniaxial-stress splitting

We have measured the stress splittings of the two main lines A and B for uniaxial stresses along the [111], [001], and [110] crystallographic directions. The most striking result is for stress along the [111] direction, where no splitting of either of the two main transitions occurs. Uniaxial stress along the [111] direction gives rise to the τ_2 modes of strain (e_{xy}, e_{yz}, e_{zx}) and to a breathing mode of strain $e_{a1}=e_{xx}+e_{yy}+e_{zz}$. The τ_2 modes couple the three orbital states of the T_1 manifold to each other. Hence, the τ_2 modes would couple the states associated with different distortions. However, as we have seen in conjunction with the spin-orbit interaction, states associated with different distortions are not in contact with each other as a result of the Jahn-Teller coupling being in the static limit. That is, the coupling to the τ_2 modes of strain is quenched by the Jahn-Teller coupling. Thus, there are no splittings resulting from the [111] stress, in agreement with our experimental results.

The breathing mode of strain e_{a1} shifts each of the states associated with the different distortions by an equal amount relative to the $^6A_1$ ground manifold. Hence there are no splittings resulting from the breathing mode of strain. We note that this mode is a result of any uniaxial stress. In analyzing experimental results, the shift due to the breathing mode of strain must be taken into consideration. As there are no splittings resulting from the [111] stress, the shift due to the breathing mode can be easily determined using the shift found from the [111] uniaxial stress.

The [001] uniaxial stress gives rise to an $e_\theta=2e_{zz}-e_{xx}-e_{yy}$ mode of strain, in addition to the breathing mode. The result of such a strain is to remove the equivalence of the three distortions by distinguishing the distortion along the stress axis, which we define to be the z axis. The shift in energy, as a function of stress, of the $^4T_{1z}$ states (associated with the distortion along the z axis) is twice as large and in the opposite sense as the shift of each of the $^4T_{1x}$ and $^4T_{1y}$ states. Hence, each of the lines A and B are split into two components, which we have labeled A_z (B_z) and A_{xy} (B_{xy}).

We can calculate the relative intensities of each of the transitions from the various excited states to the six states of the $^6A_1$ manifold. This is done by determining the matrix elements of the electric-dipole operators (x,y,z) taken between the states given in Eq. (4), the excited states, and the states given in Eq. (1), which represent the ground states.

For light collected along any direction perpendicular to the applied stress, the model predicts the following results. The components A_z and A_{xy} (B_z and B_{xy}) have the same intensity for light polarized perpendicular to the stress. There are no optical dipole transitions from the $^4T_{1z}$ states to the ground states with polarization parallel to the stress. Hence, by measuring the polarization of light perpendicular and parallel to the stress, we can determine which of the components arises from transitions starting in the $^4T_{1z}$ states. We have labeled these components A_z and B_z (see Figs. 3 and 4).

A uniaxial [110] stress, in addition to the breathing mode, gives rise to a τ_2 mode of strain (e_{xy}) and an e_θ mode of strain. As in the case of the [111] stress, the e_{xy} strain does not give rise to any splittings. The e_θ strain resulting from a given [110] stress is half as large and in the opposite sense as the e_θ strain resulting from a [001] stress of the same magnitude. Hence a [110] stress will split each of the two lines A and B into two components, the component arising from transitions starting in the $^4T_{1z}$ states (A_z,B_z) moving to higher energies with compressive stress. An analysis of the electric-dipole matrix elements shows that for light polarized parallel to the stress, and collected in any direction perpendicular to the stress, the two components from each of the lines A and B have equal intensities. For light polarized perpendicular to the stress and collected in the [001] direction, we find again that both components from each of the lines A and B have equal intensities. However, for light polarized perpendicular to the stress and collected in the [110] direction, the two components arising from transitions starting in the $^4T_{1z}$ states, those shifting to higher energies, both vanish. For uniaxial stress in the [001] and [110] directions, we find perfect agreement between the predictions of the model and our experimental results.

C. Magnetic-field splitting

The Zeeman interaction involves an orbital term and a spin term. The orbital term includes the orbital-angular-momentum operator, which mixes the states belonging to different distortions. However, in exactly the same manner as the spin-orbit interaction, the Jahn-Teller coupling in the static limit quenches the orbital term of the Zeeman interaction in the excited $^4T_1$ manifold.

The spin term of the Zeeman interaction is

$$\mathcal{H}_Z=g_e\mu_B\mathbf{H}\cdot\mathbf{S}\ , \tag{5}$$

where $g_e=2.0023$. This term is not affected by the Jahn-Teller coupling, since it operates only in spin space. By calculating the matrix elements of the spin operator $\mathbf{S}$, we can determine how a given magnetic field will act on the states [Eq. (4)] within each of the three distortions. As a particular example we consider the case of a magnetic field directed along one of the cubic axes, defined to be the z axis. We have plotted in Fig. 18(a) the splittings of the two main states coming from the $^4T_1$ manifold that result from a magnetic field along the [001] direction. In this figure, the Zeeman components coming from the $^4T_{1z}$ states are shown with a solid line; and the Zeeman components coming from the $^4T_{1x}$ and $^4T_{1y}$ states are shown with a dotted line. As shown in this figure, the spin operator S_z splits in first order each of the two pairs of states associated with the z-axis distortion. For a given magnetic field, the splitting between the states $|z,3/2\rangle\rangle$ and $|z,-3/2\rangle\rangle$ is three times as great as the splitting between the states $|z,1/2\rangle\rangle$ and $|z,-1/2\rangle\rangle$. For the two pairs of states associated with the x-axis distortion, there

is a first-order Zeeman splitting only for the states $|x,3/2\rangle\rangle$ and $|x,-3/2\rangle\rangle$. There is, however, a second-order splitting of the states $|x,1/2\rangle\rangle$ and $|x,-1/2\rangle\rangle$. In addition, the coupling between the two main states by S_z gives rise to a nonlinear splitting of the states $|x,3/2\rangle\rangle$ and $|x,-3/2\rangle\rangle$. The states associated with the y-axis distortion behave in an identical fashion to those associated with the x-axis distortion. In Figs. 18(b) and 18(c), we have plotted the splittings of the two main states coming from the $^4T_1$ manifold for a magnetic field along the [110] and [111] directions, respectively.

The Zeeman interaction also gives rise to splittings between the six states of the $^6A_1$ manifold. The Zeeman interaction within this manifold is simply that given in Eq. (5), except that g_e is replaced by the factor $g=2.0034$.[8] The difference between g and g_e is a result of the spin-orbit mixing between the $^4T_1$ and $^6A_1$ manifolds.

Since we know the splitting of the $^4T_1$ manifold and of the $^6A_1$ manifold with magnetic field, the optical transition energies can be calculated. In Figs. 6, 8, and 10 the development of the transition energy with **H** along the [001], [110], and [111] directions is plotted and compared with the experimental results. In these figures, the transitions coming from the $^4T_{1x}$ and $^4T_{1y}$ states are shown with a solid line; and the transitions coming from the $^4T_{1z}$ states are shown with a dotted line. Only allowed transitions are depicted.

For a magnetic field along the [001] direction and at $T=4.2$ K the initial states are the lowest Zeeman component originating from the $^4T_{1z}$ state and the two lowest Zeeman components originating from the $^4T_{1x}$ and $^4T_{1z}$ states [see Fig. 18(a)]. In the experiment the transitions starting from the lowest Zeeman component of the $^4T_{1z}$ state and the lowest Zeeman component of the $^4T_{1x}$ and $^4T_{1y}$ states are not resolved in the experiment due to their energy separation of only 0.1 meV. One transition shown in Fig. 6 is not experimentally detected since the transition probability is of the order of 10^{-4}.

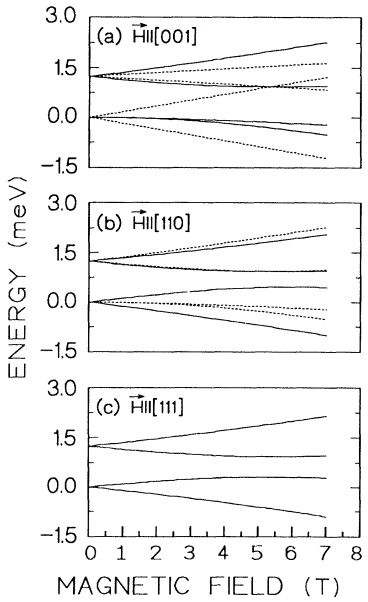

FIG. 18. Theoretical splitting of the $^4T_1$ state as a function of the magnetic field. The states originating from the distortion along the z axis are drawn as dotted lines.

In the case of a magnetic field along the [110] direction, the lowest Zeeman components coming from the $^4T_{1x}$ and $^4T_{1y}$ states and two lowest Zeeman components coming from the $^4T_{1z}$ state are involved in the optical transition [see Fig. 18(b)]. However, the transitions originating from the lowest Zeeman component of the $^4T_{1x}$ and $^4T_{1y}$ states almost coincide with the transitions originating from the second-lowest Zeeman component of the $^4T_{1z}$ state (see Fig. 8). Therefore these transitions are not resolved in the PL spectra.

For **H** along the [111] direction it is no longer necessary to distinguish between states associated with an x-, y-, or z-axis distortion since the splitting of the $^4T_{1x}$, $^4T_{1y}$, and $^4T_{1z}$ states is identical. At 4.2 K, the initial state is the lowest magnetic-field-split state of the $^4T_1$ manifold.

On the basis of Eq. (5) we have calculated the angular dependence of the optical transitions. In Fig. 12 the anisotropy of the most intensive PL lines is presented for $H=6.5$ T. Again, the transitions coming from the $^4T_{1x}$ and $^4T_{1y}$ states are shown with a solid line; and the transitions coming from the $^4T_{1z}$ state are shown with a dotted line. In order to keep Fig. 12 clear the transitions originating from the second-lowest Zeeman components of the $^4T_{1x}$ and $^4T_{1y}$ states are only traced from 70° to 90°. The PL transitions of the dotted curve marked with an arrow in Fig. 12 start from the lowest Zeeman component of the $^4T_{1z}$ state. This transition is forbidden for **H** along the [001] direction. Therefore the experimental points show a crossover from the increasingly forbidden transition to the allowed transitions from the $^4T_{1x}$ and $^4T_{1y}$ states when the angle is close to the [001] direction.

We have calculated theoretical spectra for the cases of applied magnetic fields in several directions, using the matrix elements of the electric-dipole operators to determine the allowed transitions and their polarizations. Our experimental measurements of the magnetic-field splittings were performed at 4.2 K. Due to thermalization effects, the higher-energy states from the $^4T_1$ manifold are effectively unpopulated. So, in our theoretical spectra we have used only the states that give rise to the line A. The energy positions of the various lines in the theoretical spectra are simply the energy differences between the initial and final states of the transition, assuming a magnetic-field strength of 7 T. The relative intensities and polarizations of the various lines are determined from the matrix elements of the electric-dipole operators. In addition, in order to account for the population differences in the excited states, we have included a Boltzmann factor. Finally, we have assumed a Lorentzian line shape with broadening of 0.1 meV. These theoretical spectra are shown for magnetic fields directed along the [001] axis (Fig. 13), the [110] axis (Fig. 14), and the [111] axis (Fig. 15).

As with the uniaxial stress, we find almost perfect agreement between the predictions of the model, as

shown by the theoretical spectra, and our observed spectra. This agreement is best seen for the unpolarized spectra. We note, however, that we observe for a few lines slightly different intensities compared with the theoretical prediction. Two different effects seem to be responsible for this deviation. First, the nonideal polarizer gives incorrect intensities for intense, almost totally polarized lines in the direction perpendicular to the strong polarization (see Fig. 13). Second, an inhomogeneous strain field in the samples will lead to deviations from the calculated transition probabilities. The influence of the inhomogeneous strain also leads to small intensity changes in the unpolarized spectra (see Figs. 14 and 15). A proper account of this effect is not possible at the present time.

VI. CONCLUSIONS

We have presented a model for the electronic structure of the Mn^{2+} impurity in GaP. This model includes a Jahn-Teller coupling to the ε modes of distortion within the excited $^4T_1$ manifold. We never observed splittings resulting from a tunneling between the various distortions; therefore we conclude that the Jahn-Teller coupling is in the static limit. We have demonstrated that the Jahn-Teller coupling is responsible for the merging of the four spin-orbit manifolds in the $^4T_1$ manifold into two states. Our treatment of this problem complements those of Refs. 4, 5, and 6, and allows a simple determination of the electric-dipole matrix elements between various excited and ground states. We have studied how a uniaxial stress or a magnetic field splits the two main states of the $^4T_1$ manifold. The experimental results support our model of a strong Jahn-Teller coupling to the ε modes of distortion in the excited $^4T_1$ manifold of the Mn^{2+} impurity in GaP.

ACKNOWLEDGMENTS

The authors are grateful to A. Keckes for growing the VPE GaP:Mn samples and to the Crystal Preparation Department for preparing the samples for the uniaxial-stress experiments. We appreciate the technical assistance of W. Heinz and W. Krause with the photoluminescence measurements, and we would like to thank H. J. Queisser for his interest in, and support of, this work.

[1] A. T. Vink and G. G. P. Van Gorkom, J. Lumin. **5**, 379 (1972).
[2] D. Langer and S. Ibuki, Phys. Rev. **138**, A809 (1965).
[3] D. W. Langer and H. J. Richter, Phys. Rev. **146**, 554 (1966).
[4] P. Koidl, Phys. Status Solidi **74**, 477 (1976).
[5] D. Fournier, A. C. Boccara, and J. C. Rivoal, J. Phys. C **10**, 113 (1977).
[6] R. Parrot, C. Naud, C. Porte, D. Fournier, A. C. Boccara, and J. C. Rivoal, Phys. Rev. B **17**, 1057 (1978).
[7] F. G. Anderson and F. S. Ham, in *Materials Science Forum 38-41, Proceedings of the 15th International Conference on Defects in Semiconductors, Budapest, 1989,* edited by G. Ferenczi (Trans Tech, Aedermannsdorf, 1989), p. 305
[8] R. S. Title and T. S. Plaskett, Appl. Phys. Lett. **14**, 76 (1969).